MODELING OF FLUX ROPE CORONAL MASS EJECTIONS

A. F. R. THERNISIEN

Universities Space Research Association, 10211 Wincopin Circle, Suite 620, Columbia, MD 21044; and Naval Research Laboratory, Code 7663, 4555 Overlook Avenue SW, Washington, DC 20375; arnaud.thernisien@nrl.navy.mil

R. A. HOWARD

Naval Research Laboratory, Code 7663, 4555 Overlook Avenue SW, Washington, DC 20375; russell.howard@nrl.navy.mil

AND

A. VOURLIDAS

Naval Research Laboratory, Code 7663, 4555 Overlook Avenue SW, Washington, DC 20375; angelos.vourlidas@nrl.navy.mil

ABSTRACT

We present a forward-modeling technique for flux rope–like CMEs using an empirically defined model of a flux rope, the graduated cylindrical shell (GCS). To compare it with white-light coronagraph observations, we assume an electron distribution through the GCS and derive synthetic images in total and polarized brightness for various projections of the model using a Thomson scattering ray-tracing program. We test our forward modeling technique on 34 LASCO CMEs analyzed by Cremades & Bothmer. We are able to reproduce the CME morphology and derive the electron density (at the CME front) of these events using multi-instrument observations (MDI, Hα, EIT, LASCO) under the assumption of self-similar expansion. This study suggests that a flux rope–like structure is a good description for these events. We also find that we need to invoke a deflection and/or rotation of the structure relative to the position and orientation of the source region in most cases. Finally, we demonstrate an original technique to fit the electron density of the CME leading edge. We find that, on average, the peak of the density at the CME front is 7.5 times that in the equatorial model of Saito et al., and can reach ∼22 times the model in some cases.

Subject headings: Sun: corona — Sun: coronal mass ejections (CMEs)

1. INTRODUCTION

White-light coronagraphs regularly record expulsions of plasma in the solar corona. The shapes and sizes of these so-called coronal mass ejections (CMEs) vary from event to event and have created a need to organize them based on their morphological similarities (e.g., Howard et al. 1985). Over the years, the "three-part" morphology has attracted particular attention. A typical three-part CME consists of a bright, circular front, followed by a darker area or cavity, which in turn is followed by a bright core (Illing & Hundhausen 1986). The high sensitivity of the LASCO coronagraphs (Brueckner et al. 1995) has revealed much more structure in these events. In particular, circular striations have been frequently observed in the cavities of three-part CMEs, creating the appearance of a helical or flux rope structure. Models of idealized flux ropes have been successful in reproducing the observations (Chen et al. 1997), and analysis of their properties (Vourlidas et al. 2000; Krall & St. Cyr 2005) has shown that they are consistent with theoretical flux ropes and magnetically dominated systems. In contrast, the CME ice cream cone model is not valid from a magnetically dominated system point of view. Further work has shown that the flux rope CMEs tend to expand self-similarly (Chen 1996; Chen et al. 1997, 2000). As a result of these analyses, the term "flux rope CME" has been gradually replacing the "three-part" CME because it provides a more accurate description of the white-light appearance variety of these events.

For a long time, observations of cavities above long filaments indicated these regions as the source regions of the three-part CMEs, but a conclusive result was missing until recently. Cremades & Bothmer (2004, hereafter CB04) did a systematic study of 124 flux rope CMEs (they used the term "structured" in their study) and analyzed the relationship between source region character-

istics at the surface of the Sun and the morphology of the CME observed with LASCO coronagraphs. For each of the events, they tabulated the position of the source region (SR) detected with EIT, and they measured the orientation of the SR neutral line on MDI and with Hα data. They also tabulated the corresponding position angle (PA) and angular width (AW) of the CME observed with LASCO. They found a good correlation between the neutral line position and orientation, and the CME morphology observed on LASCO: the structured CMEs seem to arise in a self-similar manner from preexisting small-scale loop systems. However, during the eruption, the flux rope is subject to the influence of coronal holes and streamers (Cremades et al. 2005), and more generally to the large-scale configuration of the corona. As a consequence, they found that CMEs are quasi-systematically deviated and/or rotated compared to the location of the SR and the orientation of the neutral line.

The CB04 study provides a consistent picture of the relation of the flux rope CMEs to their SRs. However, it does not explicitly prove that a flux rope–like structure with the measured low-corona characteristics can indeed account for the observed CME structure. This missing link is the motivation for our study. In particular, we use the CB04 tabulated data for 34 events and the assumption of self-similar expansion to create a flux rope–like model, with which we fit the LASCO observations via a forward-fitting method. We show that the low-corona measurements can indeed provide a good first guess of the position and orientation of an ejected flux rope as seen by a coronagraph. However, since the CMEs are generally deflected and rotated compared to their SR position, corrections have to be applied in order to better fit the data with our model.

After obtaining a satisfactory fit to the CME morphology, we proceed to derive the density of the front. With the single point of view provided by LASCO, it is not possible to derive the electron
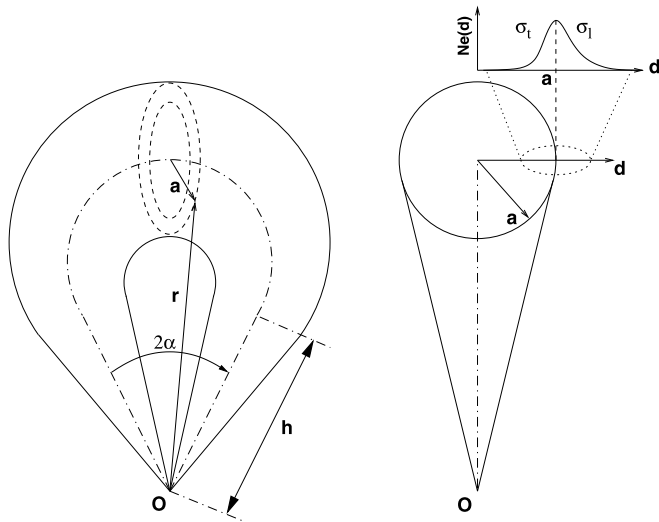
Fig. 1.—GCS face-on and edge-on representations. The dash-dotted line shows the axis through the center of the shell. The solid line represents a lengthwise planar cut through the cylindrical shell and the origin. It shows the locus of the peak of density in the shell. On the upper right, we show the electron density profile of the shell, $N_e(d)$ (see eq. [2]); σ_t and σ_l are respectively the trailing and leading falloff coefficients of the density profile. "O" corresponds to the center of the Sun.

density without making assumptions on the morphology of the density. Van de Hulst (1950) and more recently Hayes et al. (2001) or Quémerais & Lamy (2002), for example, assumed local spherical symmetry of the density in order to determine the radial density profile of the quiet K corona (streamer and coronal holes). This is the simplest assumption that can be made, and it is clearly valid in the case of the solar-minimum quiet corona. Another method, known as solar rotational tomography, has also been used on LASCO data to reconstruct the electron density of the corona (Frazin & Janzen 2002; Frazin & Kamalabadi 2005a, 2005b). This method also relies on the assumption that the corona remains constant during a Carrington rotation, which is obviously a limitation when looking at transient events like CMEs. Nevertheless, when multiple views of a CME are available, tomography techniques can be used as demonstrated in Jackson & Froehling (1995), who used *Helios* and Solwind observations to reconstruct the three-dimensional electron density of a CME. We approach this problem using a forward-modeling technique. We construct a geometric model for the structure under analysis with a certain number of free parameters. We then vary these parameters to match the observations. Such methods are more suitable when the assumption of

spherical symmetry is not valid. Thernisien & Howard (2006) implemented this technique for the reconstruction of a streamer. They assumed a slab model morphology for a portion of the streamer belt and made use of a minimization technique to derive the electron density.

In this present study, we expand this technique to LASCO CME observations to derive the electron density in the leading edge of CMEs. We point out that such a forward-modeling method will be extremely useful for locating the position of CMEs in space using the two-point viewing from the upcoming *STEREO* mission, as Pizzo & Biesecker (2004) demonstrated using a geometric model and a triangularization method. The paper continues with a description of our flux rope model in § 2, its application to the CB04 measurements in § 3, and its comparison to the observations in § 4. We discuss the results and conclude in § 5.

2. THE GRADUATED CYLINDRICAL SHELL MODEL

The graduated cylindrical shell (GCS) is meant to reproduce the large-scale structure of flux rope–like CMEs. It therefore consists of a tubular section forming the main body of the structure attached to two cones that correspond to the "legs" of the CME. The resulting shape is reminiscent of a croissant. Figure 1 shows a face-on and an edge-on representation of the model. The cross section of the model is a circular annulus of varying radius, a, given by

$$a(r) = \kappa r, \qquad (1)$$

where r the distance from the center of the Sun to a point at the outer edge of the shell, and κ is a constant depending on the studied event. For certain projection angles, the parameter κ can be viewed as the CME aspect ratio since it is the ratio of the CME size at two orthogonal directions. The tube attaches to the two conical "legs" at a height h, which is another free parameter of the model.

In Figure 1 the axis through the center of the tube is represented with the dash-dotted line, and the outline of the model is represented with a solid line. To create synthetic coronagraph images from this model, we need to prescribe a density profile. We use an asymmetric Gaussian profile along the radius a at which the density peaks at the outer surface of the shell and falls off with a different Gaussian width on either side. Namely,

$$N_e(d) = N_e \exp\left[-\left(\frac{d-a}{\sigma_s}\right)^2\right],$$

$$\sigma_s = \begin{cases} \sigma_{\text{trailing}}, & \text{if } d < a, \\ \sigma_{\text{leading}}, & \text{if } d \geq a, \end{cases} \qquad (2)$$

TABLE 1
Model and Positioning Parameters

| Parameter	Description
Model Parameters	
2α	Angular width between the "legs" of the GCS model
h...	Height of the legs
κ	Aspect ratio (see eq. [1])
N_e..	Electron density factor
σ_{trailing}	Gaussian width of the density profile in the interior of the GCS (see eq. [2])
σ_{leading} ·............................·	Gaussian width of the density profile at the exterior of the GCS (see eq. [2])
Positioning Parameters	
ϕ, θ..................................	Carrington longitude and heliographic latitude of the SR
γ	Tilt angle of the SR neutral line
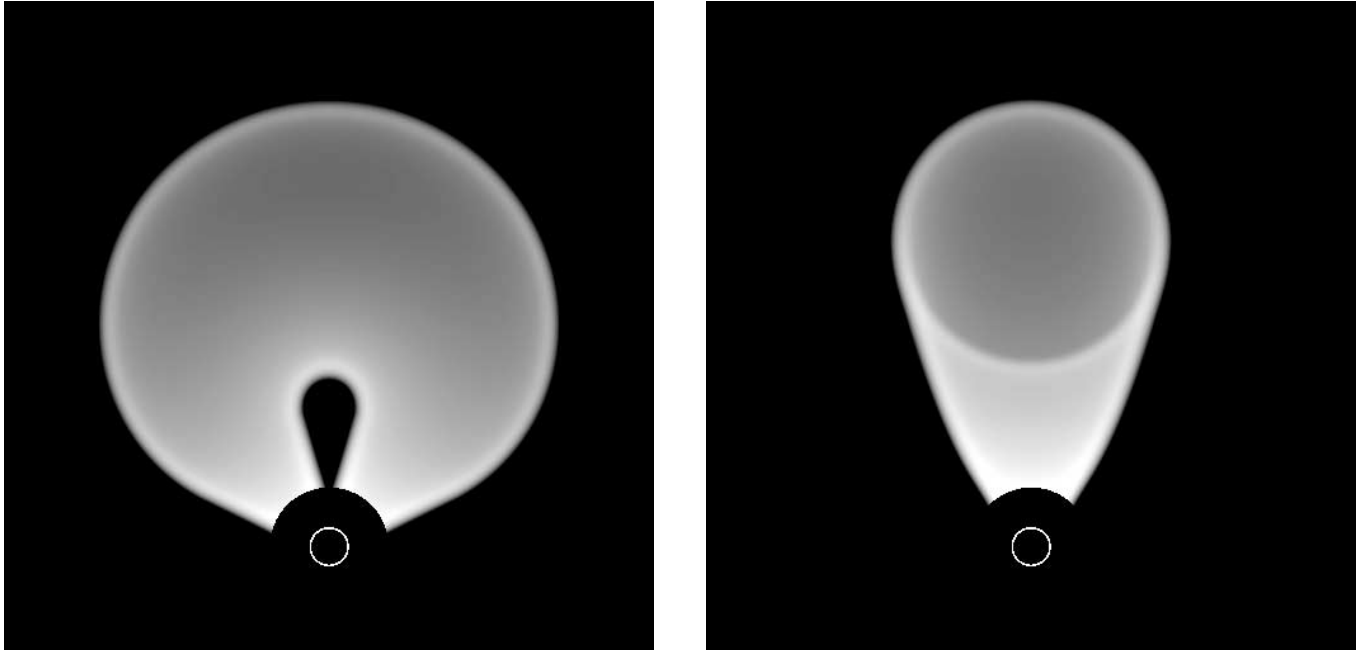
Fig. 2.—Simulated white-light images of the GCS model as seen in Fig. 1. *Left*: GCS model seen face-on. *Right*: GCS model seen edge-on.

with d the distance along the radius a from the center of the shell. Here σ_{trailing} and σ_{leading} are the widths of the Gaussian inside and outside of the shell, respectively. We find that allowing this asymmetry results in better fits to the observations.

Equation (1) implies that the model can be easily adopted to treat the CME at different heights using self-similar expansion. Under this assumption, the size of a given CME feature will scale with distance from Sun center, namely, $l = \kappa r$. In this paper we have only modeled CMEs at a single observation time.

The different parameters of the model are summarized in Table 1. Note that the leading-edge height is not an independent parameter of the model: it is a function of the height of the legs (assumed to be the same), h, the half-angular width, α, and the coefficient κ:

$$h_{\text{front}} = h \frac{1 + \kappa}{1 - \kappa^2} \frac{1 + \sin \alpha}{\cos \alpha}, \qquad (3)$$

with h_{front} the height of the CME model leading edge. Note also that the leg height h is given relative to Sun center. The photosphere is set to $1\,R_{\odot}$.

Figure 2 shows two synthetic coronagraph images of the GCS model, viewed in the same orientation as in Figure 1, face-on and edge-on, respectively. The images are generated using a ray-tracing renderer that takes full account of the Thomson scattering equations (see Appendix). Figure 2 shows that the brightest features in the simulated images correspond to the location of density peak in equation (1). The legs in the synthetic images (Fig. 2, *left*) look bigger than what is generally observed in real data. Here we are only interested in reproducing the general morphology of the CME and the density at the front. For computational simplicity, we adopt the linear function shown in equation (1) for our shell cross section. We note that there exist other parameterizations for the cross section of a flux rope–like structure (e.g., Chen et al. 2000) that can improve the agreement with observations regarding the legs of the CME.

Figure 3 shows how we locate our GCS model in 3D space with respect to the solar surface. Most of the position parameters are taken from the observations of the neutral line of the SR for

our modeled CME. The model is positioned normal to the photosphere with the legs at the opposite ends of the neutral line. The neutral line is centered at a given Carrington longitude ϕ and latitude θ with a tilt γ relative to the solar equator. A summary of all the free parameters of the model can be found in Table 1.

3. MODELING BASED ON CB04 MEASUREMENTS

3.1. *Selection of the Events*

Our starting point is the 124 CMEs studied by CB04. We first picked those events that showed clear agreement with the neutral-line orientation according to CB04. Then we used the LASCO movies of these events to discard those with overly complicated structures and weak, undefined CME fronts. Since our GCS model is simple, we are only interested in replicating the large-scale
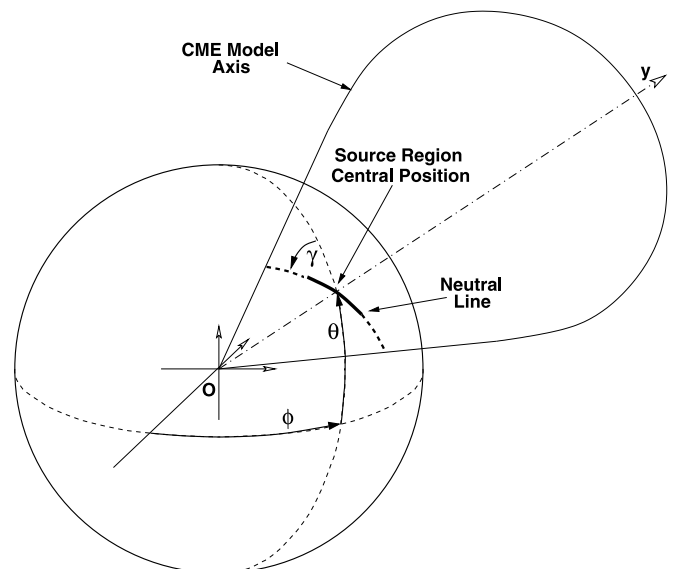

Fig. 3.—Location of the GCS model in 3D space based on observations of the SR neutral line.

TABLE 2
LIST OF THE EVENTS WE MODELED

Date, Time (UT) (1)	ϕ (deg) (2)	$\Delta\phi$ (deg) (3)	θ (deg) (4)	$\Delta\theta$ (deg) (5)	γ (deg) (6)	$\Delta\gamma$ (deg) (7)	α (deg) (8)	$\Delta\alpha$ (deg) (9)	Ori (10)	κ (11)	N_e (10^4 cm^{-3}) (12)	h ($R_\odot$) (13)	σ_t (14)	σ_l (15)	PA (deg) (16)	ρ ($R_\odot$) (17)
1997 Oct 16, 23:53	282	...	−30	16	43	55	22.1	...	EO	0.42	20.7	1.81	9.8E−2	2.4E−1	344.9	4.48
1998 Apr 23, 05:55	138	...	−18	10	24	...	19.1	...	FO	0.43	173.0	1.47	2.7E−3	1.8E−1	187.6	3.62
1998 May 19, 11:02	304	...	20	...	27	80	23.7	...	EO	0.43	4.7	2.35	4.6E−1	3.4E−1	36.3	5.31
1998 Jun 02, 10:29	179	...	−54	26	73	...	33.9	...	EO	0.28	46.7	1.70	3.3E−1	1.8E−1	327.7	4.25
1999 May 30, 12:26	32	...	−16	23	34	50	21.7	...	EO	0.38	23.4	2.14	6.7E−3	2.6E−1	347.1	3.74
1999 Jun 02, 21:50	24	...	29	−10	44	...	24.4	...	...	0.43	38.9	1.52	5.7E−1	2.6E−1	26.0	4.00
1999 Jun 11, 11:50	76	...	38	15	8	60	21.4	...	...	0.43	9.2	2.12	8.2E−2	2.5E−1	124.2	5.56
1999 Jun 16, 05:30	12	...	32	...	56	30	23.3	...	EO	0.43	6.9	2.16	8.9E−2	2.0E−1	146.8	5.77
1999 Jul 25, 14:06	32	...	39	−10	40	...	20.0	...	...	0.43	11.2	2.42	1.7E−1	2.0E−1	34.5	6.02
1999 Oct 13, 11:26	313	10	44	15	74	−55	23.0	...	EO	0.43	33.9	2.01	1.4E−1	8.0E−2	100.4	4.79
2000 Jun 25, 08:30	259	...	14	−14	67	20	21.5	...	EO	0.43	4.2	2.97	4.6E−2	2.4E−1	337.2	6.03
2000 Sep 12, 12:30	242	...	18	...	56	...	24.2	...	...	0.43	44.4	2.69	2.4E−1	2.1E−1	251.1	4.54
2000 Nov 01, 17:26	251	...	−15	−20	85	...	21.1	...	...	0.43	18.9	2.38	3.6E−2	1.6E−1	214.5	5.30
2000 Nov 04, 02:50	331	...	−32	−8	79	...	29.7	...	EO	0.43	62.2	1.56	1.1E−1	1.8E−1	321.9	4.71
2000 Nov 08, 23:26	250	...	22	...	25	...	18.8	...	...	0.43	20.5	2.60	4.6E−4	2.3E−1	28.2	5.69
2000 Nov 23, 21:30	296	...	−32	−5	12	...	21.5	...	...	0.43	26.7	2.02	1.3E−1	1.8E−1	217.5	4.99
2001 Apr 01, 11:50	358	...	−23	...	20	...	19.7	...	FO	0.43	17.5	2.35	9.7E−2	2.8E−1	211.8	5.75
2001 Apr 23, 21:30	240	...	−33	...	71	...	22.7	...	...	0.43	10.0	2.28	3.7E−1	2.1E−1	325.3	5.78
2001 May 15, 19:29	140	...	24	12	51	40	24.2	...	EO	0.52	11.9	2.12	1.3E−1	1.1E−1	166.3	5.71
2001 Jun 26, 12:54	316	...	−12	2	5	85	15.6	...	EO	0.52	12.4	1.72	1.8E−2	3.9E−1	196.8	4.79
2001 Jul 23, 10:27	142	...	6	15	0	85	17.5	...	EO	0.42	11.9	2.38	3.8E−1	2.8E−1	18.2	5.48
2001 Aug 09, 22:06	77	...	−20	−12	50	...	28.7	...	...	0.43	52.2	1.74	3.0E−1	1.5E−1	186.0	4.20
2001 Aug 21, 13:27	74	...	−22	10	64	...	21.6	...	...	0.43	26.6	2.36	1.6E−1	3.2E−1	309.2	4.35
2001 Nov 01, 15:06	80	...	−20	−5	9	...	18.0	...	FO	0.43	71.3	2.04	3.9E−2	1.1E−1	220.8	4.75
2001 Dec 20, 01:54	201	...	−21	5	57	...	30.4	...	EO	0.28	19.9	2.81	9.3E−2	1.0E−1	205.6	5.35
2001 Dec 28, 20:30	18	...	22	...	25	...	20.9	...	FO	0.28	71.0	2.30	1.6E−1	2.0E−1	169.4	4.27
2002 Jan 04, 10:06	326	...	25	15	62	...	26.9	...	EO	0.43	86.9	1.48	2.0E−1	2.8E−1	144.5	4.02
2002 Mar 02, 16:06	273	...	−24	...	56	...	31.7	...	...	0.43	23.3	1.95	4.3E−2	2.8E−1	197.9	6.13
2002 Mar 18, 03:30	178	...	−9	5	12	...	22.2	...	...	0.43	39.4	2.93	3.6E−2	1.6E−1	20.4	4.81
2002 May 21, 22:26	344	...	20	3	37	−70	18.8	...	...	0.43	63.8	2.16	9.0E−2	3.5E−1	126.1	4.20
2002 May 22, 00:26	89	...	16	...	48	...	19.5	10	...	0.43	33.2	1.62	3.0E−2	1.3E−1	340.2	4.66
2002 Aug 01, 06:30	141	20	−22	...	7	−5	21.1	...	EO	0.43	26.6	2.50	8.6E−2	4.5E−1	265.6	4.39
2002 Aug 13, 11:30	292	...	40	8	75	...	21.1	...	EO	0.43	10.6	2.58	1.5E−1	2.9E−1	134.2	6.27
2002 Oct 15, 15:06	225	20	−25	...	90	90	36.6	...	EO	0.43	12.7	1.84	3.8E−1	9.9E−2	273.7	4.74

NOTES.— Position and orientation of the SR are from CB04. Col. (1): Date and time of the LASCO C2 image used for the fit. Cols. (2) and (3): Carrington longitude and heliographic latitude of the SR. Cols. (4) and (5): Correction to the longitude and latitude, if any. Cols. (6) and (7): Tilt angle of the SR neutral line and correction. Cols. (8) and (9): Half-angle width of the model and correction. Col. (10): GCS orientation (EO for edge-on, FO for face-on). Col. (11): Cross section aspect ratio. Col. (12): Electron density peak value. Col. (13): Height of the legs. Cols. (14) and (15): Inner and outer Gaussian widths for the density profile. Col. (16): Position angle of the density fit. Col. (17): Radial position of the density fit.

structure of the CME and not fine features within it. Finally, we ended up with 34 CMEs to apply our forward-modeling technique on. The selected events are listed in Table 2.

3.2. Method

We proceed in two steps. In the first step, we use assumptions and information provided by different instruments to define the values of some of the GCS model parameters. In the second step, we compare the simulated CME with LASCO observations and refine, first manually, then automatically, the remaining parameters. We consider only one LASCO image at a time for the fitting. To study a time sequence, we would have to repeat the last step for each image in the sequence.

3.3. Assumptions and Use of Source Region Morphology Information

LASCO provides a 2D projection of a 3D structure. Due to these projection effects, some of the model parameters cannot be determined unambiguously. Therefore, we need to introduce some assumptions and make use of the information provided by instruments other than LASCO, such as EIT or MDI. Our main assumption concerns the expansion of the CME, which we consider to be self-similar: the position, length, and orientation of the SR neutral line associated with an event will characterize the morphology of the CME expansion. This implies that the SR has to be visible when imaging the solar surface in order to determine its position and orientation.

TABLE 3
AVERAGE ASPECT RATIO FOR EACH OF THE SIX SELECTED EDGE-ON EVENTS

Date	$\bar{\kappa}$	σ_κ	Number of Measurements
1997 Oct 16	0.46	4.9E−2	4
1998 Jun 02	0.31	7.4E−2	4
1999 Jun 16	0.42	1.5E−2	4
2001 May 15	0.52	...	1
2001 Jun 26	0.48	8.0E−2	4
2001 Jul 23	0.44	2.5E−2	4
Overall mean	0.43	7.5E−2	21

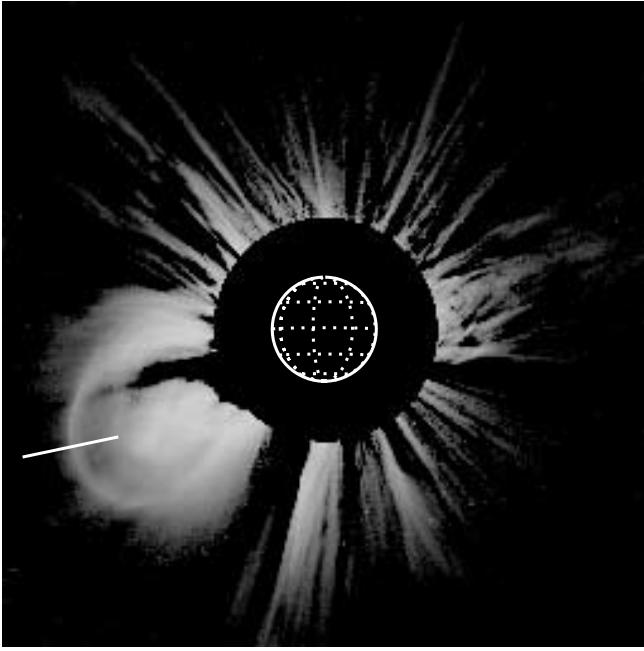NOTE.— The last line gives the statistics for the entire population.

FIG. 4.—Example of LOS profile (*straight line segment*), $p_r(\rho)$, along which we perform the electron density inversion, here for the event of 2001 December 20.

As mentioned in the introduction, CB04 studied 124 structured CMEs and have uniquely identified their SRs. We use their measurements of the SR position and orientation as an input for our modeling. Here is the list of assumptions we made and the corresponding parameters of the model.

1. We assume that the CME expands radially along the line defined by the center of the Sun and the SR position. This line corresponds to the axis of symmetry of our model, denoted O−y in Figure 3. That position is given by the Carrington longitude ϕ and heliographic latitude θ of the SR.

2. We assume that the orientation of the GCS is given by the orientation angle of the SR neutral line, denoted γ. We also as-

sume that the tube remains in that orientation during its expansion. We later discuss how that assumption compares with the observations.

3. We assume that the angular width (AW) of the CGS is related to the length of the SR neutral line. To determine the relationship between the neutral line length and the CME width, CB04 selected events with neutral lines closely parallel to the west limb to reduce the influence of the projection effects. They found that even though the neutral line length and the CME width are correlated, there is considerable scatter in the data. The scatter is probably due to some residual projection effects and to a dependency between the SR lifetime and the dynamics of the CME (see CB04). Nevertheless, CB04 were able to derive a linear relationship between AW and SR length: AW = 0.84 length$_{SR}$ + 79. We use this relation to set the AW of our CGS model. When the modeled event was seen face-on, we were able to correct the AW to match the observations.

3.4. *Fit to Observations*

Once the different model parameters using the SR position and morphology are set, we compare the Thomson scattering rendered image with the observed data from LASCO. The remaining undetermined parameters are the CME height, the self-similarity expansion coefficient κ, and the shell skin density profile.

Our simulations show a very good alignment with the LASCO observations in only six of the 34 cases studied. The CME expansion is obviously not as simple as the assumption of self-similarity made here. Even though the agreement was generally good in the majority of the cases, we had to change the location and orientation of the SR to improve the match to the observations. These corrections were applied manually. We did not adjust any parameters that were impossible to determine due to the projection effects. For example, we did not adjust the AW if the CME was observed edge-on. The manual fit was based on the following adjustments:

1. The CME height, which is controlled by the parameter h (see Table 1).

2. The latitude θ when the SR is located near the eastern or western limb.
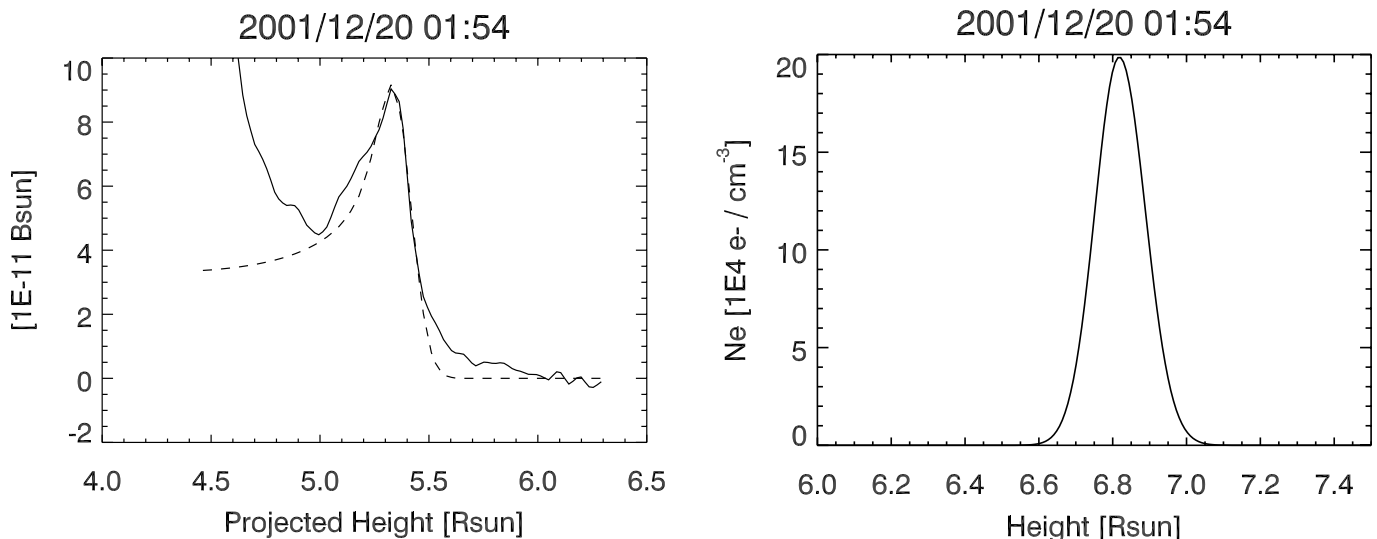

FIG. 5.—Result of the fit for the CME of 2001 December 20 corresponding to the profile displayed in Fig. 4. *Left*: Brightness profile. The solid line and the dashed line are the LASCO C2 data and the reconstructed brightness from the GCS model, respectively. *Right*: Corresponding electron density profile across the shell skin. Note that the abscissa is the radial, true height along the GCS model and that the density profile corresponds to the density at the "true" leading edge of the CME.
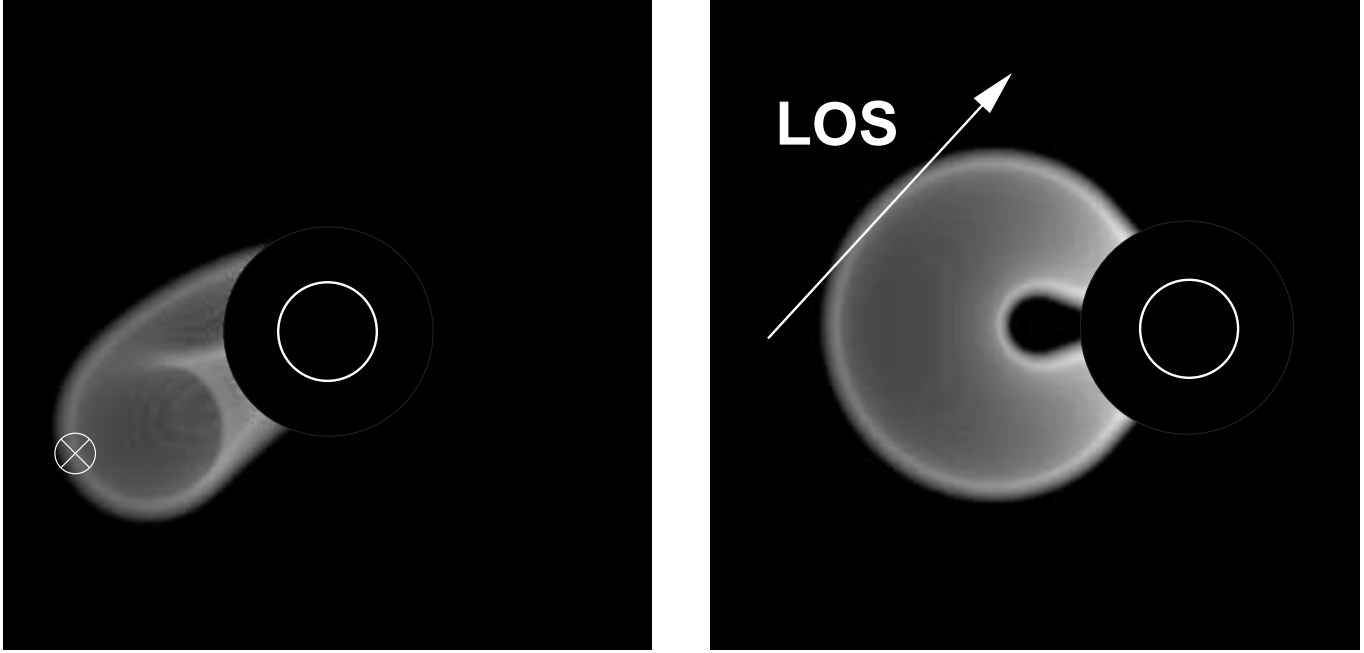
Fig. 6.—*Left*: GCS modeled CME of 2001 December 20, as seen from LASCO C2. The circle with the cross inside represents the LOS vector; in this view it is perpendicular to the image plane. *Right*: The same modeled CME, but now seen from the solar north. The vector represents the LOS of the image on the left.

3. The tilt angle γ and the aspect ratio κ when the loop is observed edge-on.

4. The longitude ϕ when the loop is located near the northern or southern limb.

5. The half-angular width α when the loop is observed face-on.

Such corrections have some observational basis. For example, MacQueen et al. (1986) measured the direction of propagation of 29 *Skylab* CMEs and 19 *SMM* CMEs. They found that CMEs are often deflected (2°.5 on average) due to the influence of the background coronal magnetic and flow pattern. More recently, Cremades et al. (2005) found an influence of streamers and of the fast solar wind emanating from coronal holes on the deflection of the CMEs with respect to their associated SR. EIT observations often show twisting and rotation of the filament (when it is observed) with respect to the neutral line orientation. Krall et al. (2006) studied the property of the 2003 October 28 CME and found that the orientation of the magnetic axis of the flux rope rotated through approximately 50° as it expanded from the solar surface to 1 AU.

3.5. *Fit of the Aspect Ratio*

The fit of the aspect ratio κ is possible when the flux rope CME is seen edge-on and the SR is located on the limb. We selected the events that were within 20° from the limb, on the visible side of the solar disk. We found only six events complying with both criteria. To improve the measurement statistics we performed the fit for the whole LASCO C2 image sequence and on one LASCO C3 image. Note that the fit using LASCO C3 can only be done when the CME is still at low altitude since the signal-to-noise ratio drops considerably above about 15 $R_\odot$.

Table 3 gives the summary of the results. We can see the average aspect ratio $\bar{\kappa}$ has some scatter. Looking at the measurements for a given event, we also notice that κ tends to increase slightly with respect to the height of the CME leading edge. Nevertheless, this behavior cannot be established at this moment given the low number of measurements. The average aspect ratio and standard deviation for all six events is $\bar{\kappa} = 0.43 \pm 0.08$.

When the flux rope is not seen edge-on, it is impossible to measure the aspect ratio. In those cases, we use the average value mentioned above. Chen et al. (2006) also measured the CME aspect ratio for their modeling and study. Based on physical considerations (Chen et al. 1997), the bright rim apex of the flux rope corresponds to the maximum extension of the poloidal magnetic field B_p (circulating perpendicularly to the flux rope axis) of their model. They measured an aspect ratio[1] of $\kappa = 0.43 \pm 0.06$, which is very close to our measurement. This result suggests that our geometrical interpretation of a flux rope is very close to a physics-based description of one.

3.6. *Electron Density Fit*

The technique relies on the inversion of the equation describing the relation between the observed Thomson scattering brightness and the electron density (Billings 1966):

$$B = C \int_{\mathrm{LOS}} N_e(\boldsymbol{r}) G(r, \Omega) dz, \qquad (4)$$

where C is a constant, $G(r, \Omega)$ is a geometric function of the vector position of a point in the corona, $\boldsymbol{r}$, with r its magnitude, and of the angle Ω defined by the angle between the line joining the solar center to a point of the line of sight (LOS) and the LOS itself.

In the GCS model, the electron density is controlled by only three parameters, as described in § 2: $N_{e,\max}$, $\sigma_{\mathrm{trailing}}$, and $\sigma_{\mathrm{leading}}$. We could imagine more elaborated geometric functions to describe finer details of the density, but this would not make any physical sense since we only have one point of view for the moment: the projection effects make it impossible to locate unambiguously the depth of the density structures along the line of sight. The GCS model allows us to fit locally the electron density along profiles perpendicular to the CME front. Let $p_r(\rho)$ be such a profile, with ρ the impact parameter, defined as the distance

---

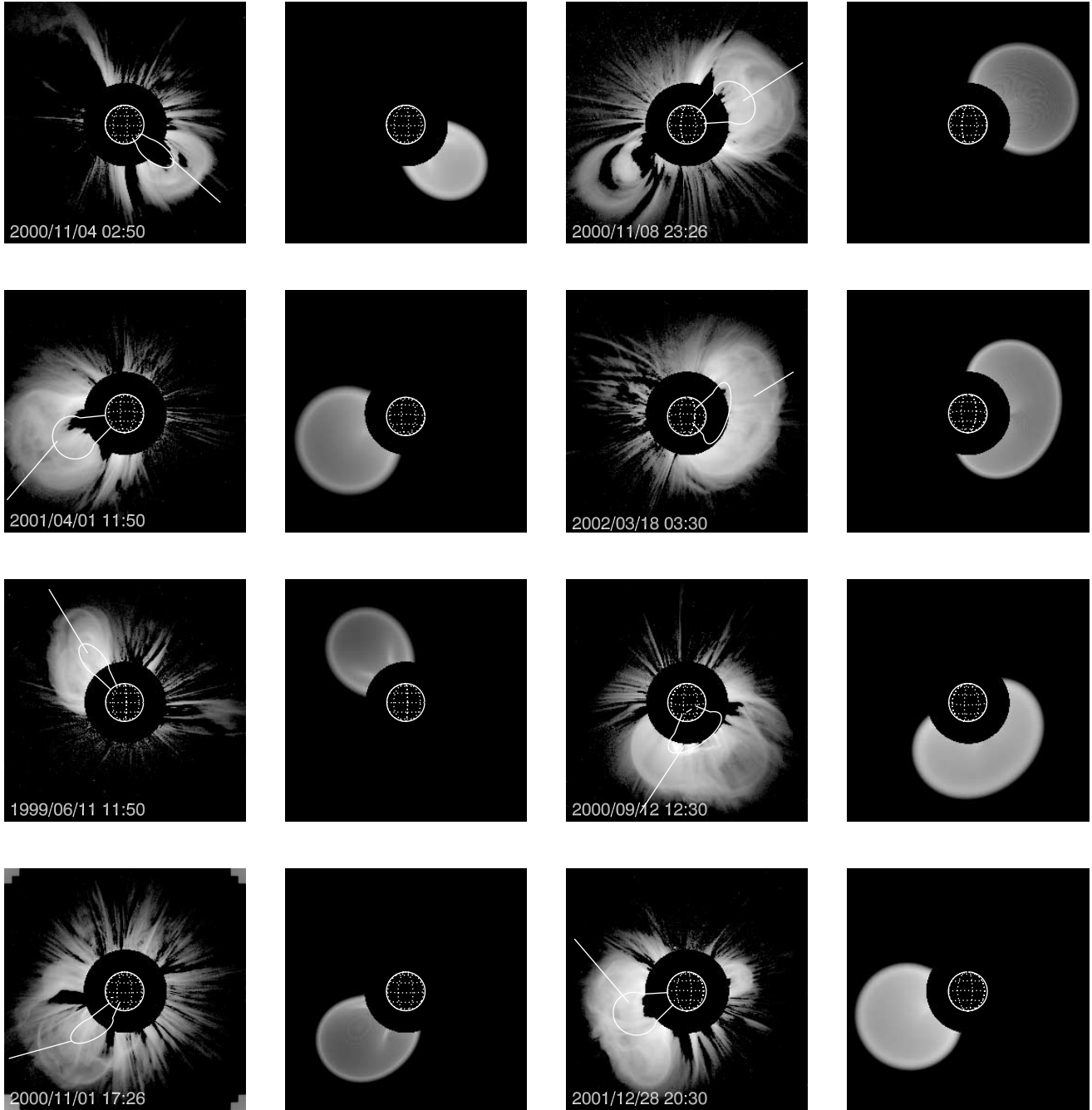[1] Actually they use the inverse of our aspect ratio, which they call $\alpha = 2.3 \pm 0.3$.

FIG. 7.—Example results from the forward-modeling technique for four events with good agreement (*top two rows*) and for four events where we found the weakest agreement (*bottom two rows*). The GCS axis and the profile used for the fit are shown in the LASCO images.

from a LOS to the center of the Sun. Figure 4 shows an example for the CME of 2001 December 20, where $p_r(\rho)$ is represented by the white line. The fit consists of iteratively computing the total brightness profile from the modeled electron density and comparing it to the LASCO observation, minimizing a χ^2 error criterion:

$$\hat{\boldsymbol{v}} = \operatorname{argmin}_{\boldsymbol{v}} \chi^2, \qquad (5)$$

where

$$\chi^2 = \sum_{i=1}^{n} \frac{[p_r(\rho_i) - \tilde{p}_r(\boldsymbol{v}, \rho_i)]^2}{\sigma_i^2}, \qquad (6)$$

with n the number of pixels in the profile, $\tilde{p}_r(\boldsymbol{v}, \rho)$ the reconstructed profile, σ_i the standard deviation of the noise in the data, and finally $\boldsymbol{v}$ the vector of parameters to be fit, which are $N_{e,\max}$, $\sigma_{\mathrm{trailing}}$, $\sigma_{\mathrm{leading}}$, and h (see Table 1).

First, the fit is done manually and then becomes automatic by using a Powell minimization method (Press et al. 1996) to minimize the criterion of equation (5). That algorithm iteratively reaches the minimum using mutually conjugate directions. The criterion must be convex to avoid being trapped in a local minimum. Tests are done by starting with different initializations of the coefficients, and the algorithm always converges toward the same solution, meaning that the criterion appears to be convex.

In practice, the number of pixels n used is small, varying generally from 10 to 20, and the images are resized to 256×256. We
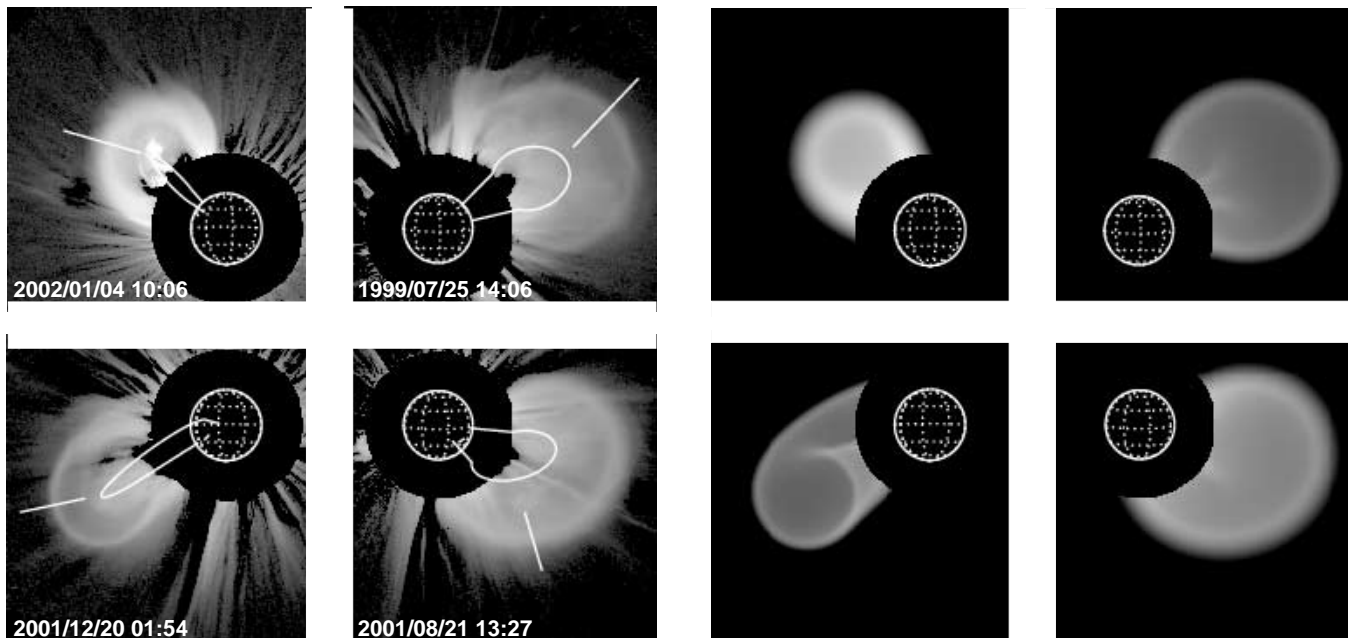
Fig. 8.—Comparison between four LASCO C2 events (*left*) and the corresponding modeling (*right*). These examples are the same as in CB04.
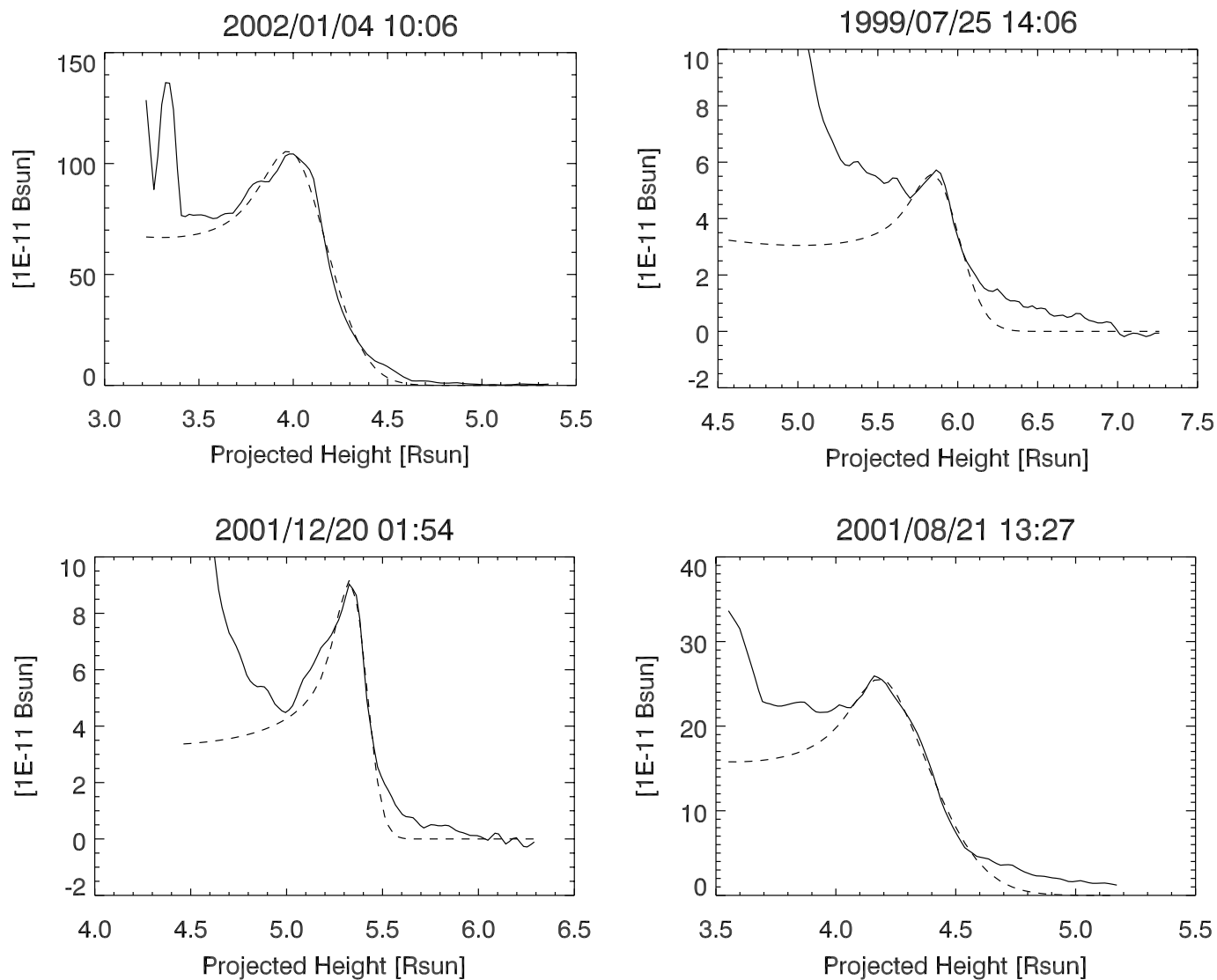

Fig. 9.—Comparison between observed and simulated brightness profiles. The layout and the events correspond to Fig. 8. The solid line is the LASCO data profile, and the dashed line is the fit.
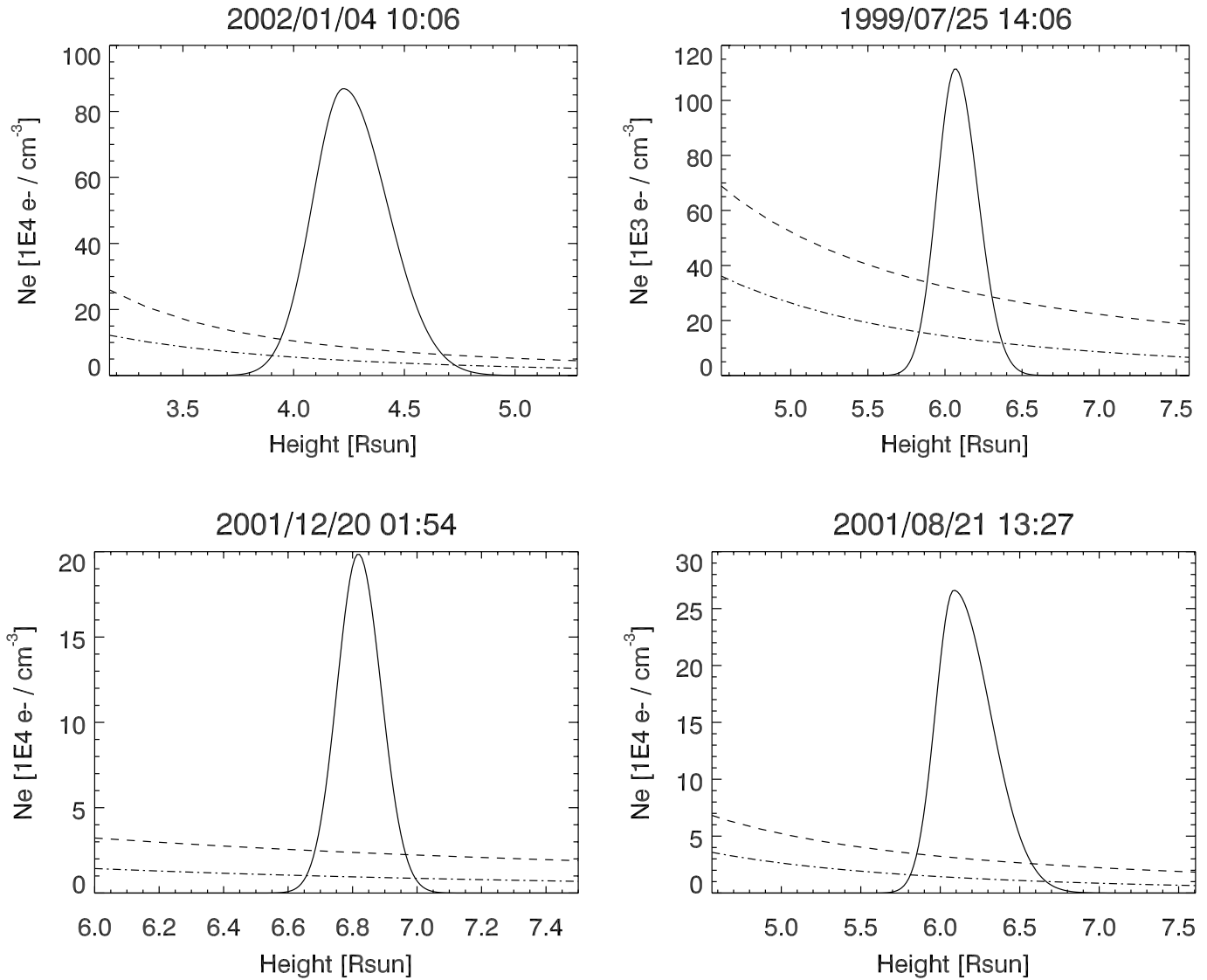
2002/01/04 10:06

1999/07/25 14:06

2001/12/20 01:54

2001/08/21 13:27

FIG. 10.— Density profiles corresponding to Fig. 9. Dashed lines and dash-dotted lines are the Saito et al. (1977) equatorial and coronal hole models, respectively. The four plots demonstrate positive skewness; the inner part of the bell-shaped curve is steeper than the front part.

try in principle to perform the fit on the brightest edge of the CME front, where the signal-to-noise ratio (S/N) is good. For the resized images where a pre-event background image has been subtracted, the typical values for the S/N are from 40 to more than 200. Since the S/N is high, we chose to set the weights σ_i of equation (6) to 1.

Figure 5 shows the result of the fit for the CME of 2001 December 20. The left panel in Figure 5 is the fit of the brightness profile. The solid line and the dashed line are respectively the LASCO C2 data and the reconstructed brightness from the GCS model. Note that we only focus on the leading edge of the CME since our model does not take into account the prominence material. The right panel of Figure 5 shows the corresponding profile of electron density across the shell skin.

3.7. *Projection Effects*

Once we determine and fit the different parameters of the model, we can view our model for different lines of sight. In Figure 6 (*left*) is the GCS modeled CME of 2001 December 20, as seen from LASCO C2. The encircled cross symbol represents the

LOS that is perpendicular to the plane of the image in this view. On the right panel is displayed the same modeled CME but now seen face-on. The LOS corresponding to the left panel is plotted, showing that the leading edge in the C2 image does not actually correspond to the "real" leading edge of the CME. This shows that our method can be used to correct projection effects in the determination of the CME front in height-time plots and therefore improve the reliability of the speeds derived from such plots. Such corrections will of course be model-dependent.

4. COMPARISON WITH THE DATA AND DISCUSSION

4.1. *Morphology*

The results of the fits are gathered in Table 2. As an example, Figure 7 shows a comparison between LASCO C2 data and the corresponding modeled image for eight sample events. The GCS axis is overplotted in the C2 image to demonstrate the orientation and position of the loop. The straight lines show the profiles that have been used to perform the electron density fit (see § 4.2). The bottom four events in Figure 7 are those where we found the weakest agreement: in these cases the edges of the observed CME

are either not nicely structured or not clearly defined. Nevertheless, the agreement remains acceptable. Figure 8 also shows the comparison for four other events that have been used as examples in CB04. To summarize, in the 12 examples presented here, as well as in the rest of the 34 studied events, the visual agreement is good, showing that the GCS morphology is a fairly good assumption in reproducing the observations.

4.2. *Electron Density*

The method to determine the electron density is described in § 3.6. Figure 9 shows four brightness profiles of a front edge corresponding to the CMEs in Figure 8. The solid and dashed lines are respectively the C2 data and the model fit. We chose an area of the CME edge that was bright and cleanly defined. We can see that the model reproduces fairly well the peak of brightness that corresponds to the bright edge of the CME.

The electron density corresponding to the Figure 9 profile fits is shown in Figure 10. The abscissa axis is in units of the true radial distance from the Sun center since we plot the density as if it were at the leading edge of the model. The dashed line and dash-dotted line are respectively the Saito et al. (1977) electron density model for the streamer belt and the coronal hole. The plots show that the CME front presents a density increase relative to the standard streamer density. On average, we found that the density maximum in the CME front is 7.54 (4.74) times the Saito et al. equatorial model, and can go up to 22.1 (11.7) times for the 2000 September 12 event, for example. The first density value corresponds to the CME leading edge according to the GCS model, while the value in parentheses corresponds to the projected front height (see Fig. 6). These can be considered as the upper and lower limits to the true density of the front.

As presented in § 2 and equation (2), the parameterization of the bell-shaped function used for the CME shell edge allows asymmetry, or skewness. In the four plots of Figure 10, the trailing part of the shell is always steeper than the leading part, demonstrating a positive skewness. We found that 24 events have this behavior. Our model assumes that the density in the front is homogeneous, which might be a strong assumption since the flux rope is supposed to be an arcade of filamentary magnetic loops. The resulting asymmetry can be an artifact of the modeling: the fitting process counterbalances the contribution of the lines of sight crossing a deeper volume of the CME shell edge by reducing the density in the inner part of that shell. Our electron density estimate is then an average along the line of sight.

Concerning the accuracy of the fit, there are two more aspects to consider: the first is the error inherent to the fitting method, and the second is the error due to the modeling choice. In our study it is clearly the second contribution that is predominant for the reasons given in the previous paragraph. Note that if the actual density distribution is more filamentary, the density contrast of these bright filaments would be even higher than what we estimate here.

In most of the 34 cases studied, it seems that there are two phases in the leading-edge density falloff. Looking at Figure 9, we see that even though the model fits well through the curve

peak, there is a slope break at larger heights that is not reproduced by the model. The smoother slope could be the signature of a snowplow effect, whose demonstration is beyond the scope of this paper.

5. CONCLUSION

We have implemented a simple modeling method to simulate the general morphology of flux rope CMEs, based on measurements of SR locations and CME orientation. We have selected from the CB04 study 34 CMEs with the simplest morphologies and the best-defined fronts. We used as modeling input the CB04 measurements of the SR morphology. Assuming self-similar expansion and using a Thomson scattering ray-tracing program, we were able to simulate the CMEs as they were seen by the LASCO C2 coronagraph. Concerning the general morphology, we found that the correlation between SR position and CME location was always very good. Nevertheless, in many of the events we had to apply corrections in order to better match the data, indicating that the CME tends to slightly deviate from the Sun center–SR axis (up to $26°$), and to rotate compared to the SR orientation (up to $90°$). After applying those corrections, the agreement between simulation and observation was good, demonstrating that the assumption of flux rope morphology is valid for these events.

Using our technique, we were also able to fit the electron density profile of the CME leading edge. We found that the peak of density was on average 7.5 times the electron density of the Saito et al. (1977) equatorial model, and was more than 22 times this model in the case of the 2000 September 12 CME. We also found that a large majority of the studied events presented a positive skewness in the density profile of the leading edge: the trailing part of the front was steeper than the leading part.

Finally, further assumptions and corrections had to be made in order to fit the observations. Some parameters, such as the angular width, when the CME is seen edge-on, cannot be accurately estimated due to projection effects. The NASA *STEREO* mission, due to launch in 2006, will provide two simultaneous viewpoints of the same event. Using forward-modeling methods on *STEREO* observations (Pizzo & Biesecker 2004) will certainly permit a reduction in the number of assumptions and allow better determination of some parameters of the model.

APPENDIX

RAY TRACING

The ray-tracing program we used (Thernisien et al. 2004) is based on the work of Bohlin & Garrison (1974). It is a numerical implementation of Thomson scattering applied to the solar corona (Billings 1966). It allows an electron density model to be placed in 3D

space with respect to both the Sun and the observer (*SOHO*, for example), and then generates an image of that scene from the observer's point of view. The core of the program is implemented in C++. Classes permitting the manipulation of vector and matrix operations have also been used, allowing users to implement their own electron density models. A graphical user interface has been implemented in IDL with useful visualization features such as 3D positioning of the models, changing the observer's point of view, and movie making. The ray-tracing software including the GCS model will be available as part of the SECCHI SolarSoft library.

REFERENCES

Billings, D. E. 1966, A Guide to the Solar Corona (New York: Academic Press)

Bohlin, J. D., & Garrison, L. M. 1974, Sol. Phys., 38, 165

Brueckner, G. E., et al. 1995, Sol. Phys., 162, 357

Chen, J. 1996, J. Geophys. Res., 101, 27499

Chen, J., Marqué, C., Vourlidas, A., Krall, J., & Schuck, P. W. 2006, ApJ, in press

Chen, J., et al. 1997, ApJ, 490, L191

———. 2000, ApJ, 533, 481

Cremades, H., & Bothmer, V. 2004, A&A, 422, 307 (CB04)

Cremades, H., Bothmer, V., & Tripathi, D. 2005, Adv. Space Res., in press, doi: 10.1016/j.asr.2005.01.095

Frazin, R. A., & Janzen, P. 2002, ApJ, 570, 408

Frazin, R. A., & Kamalabadi, F. 2005a, ApJ, 628, 1061

———. 2005b, Sol. Phys., 228, 219

Hayes, A. P., Vourlidas, A., & Howard, R. A. 2001, ApJ, 548, 1081

Howard, R. A., Sheeley, N. R., Jr., Michels, D. J., & Koomen, M. J. 1985, J. Geophys. Res., 90, 8173

Illing, R. M. E., & Hundhausen, A. J. 1986, J. Geophys. Res., 91, 10951

Jackson, B. V., & Froehling, H. R. 1995, A&A, 299, 885

Krall, J., & St. Cyr, O. C. 2005, ApJ, submitted

Krall, J., Yurchyshyn, V. B., Slinder, S., Skoug, R. M., & Chen, J. 2006, ApJ, 642, 541

MacQueen, R. M., Hundhausen, A. J., & Conover, C. W. 1986, J. Geophys. Res., 91, 31

Pizzo, V. J., & Biesecker, D. A. 2004, Geophys. Res. Lett., 31, L21802

Press, W., Teukolsky, S., Vetterling, W., & Flannery, B. 1996, Numerical Recipes (2nd ed.; Cambridge: Cambridge Univ. Press)

Quémerais, E., & Lamy, P. 2002, A&A, 393, 295

Saito, K., Poland, A. I., & Munro, R. H. 1977, Sol. Phys., 55, 121

Thernisien, A. F., & Howard, R. A. 2006, ApJ, 642, 523

Thernisien, A. F., Patel, N. S., Howard, R. A., Marqué, C., & Vourlidas, A. 2004, Fall Meeting Abstracts (Washington, DC: AGU), B404

van de Hulst, H. C. 1950, Bull. Astron. Inst. Netherlands, 11, 135

Vourlidas, A., Subramanian, P., Dere, K. P., & Howard, R. A. 2000, ApJ, 534, 456